Nature Communications

https://doi.org/10.1038/s41467-026-69661-0

Article in Press

Phase diagram and spectroscopic signatures of a supersolid in the quantum ising magnet $K_2Co(SeO_3)_2$

Received: 3 November 2025

Accepted: 5 February 2026

Cite this article as: Chen, T., Ghasemi, A., Zhang, J. *et al.* Phase diagram and spectroscopic signatures of a supersolid in the quantum ising magnet $K_2Co(SeO_3)_2$. *Nat Commun* (2026). https://doi.org/10.1038/s41467-026-69661-0

Tong Chen, Alireza Ghasemi, Junyi Zhang, Liyu Shi, Zhenisbek Tagay, Youzhe Chen, Lei Chen, Eun Sang Choi, Marcelo Jaime, Minseong Lee, Yiqing Hao, Huibo Cao, Barry L. Winn, Andrey A. Podlesnyak, Daniel M. Pajerowski, Ruidan Zhong, Xianghan Xu, N. P. Armitage, Robert Cava & Collin Broholm

Phase Diagram and Spectroscopic Signatures of a Supersolid in the Quantum Ising Magnet $K_2Co(SeO_3)_2$

Tong Chen[1,*,@], Alireza Ghasemi[1,*], Junyi Zhang[1], Liyu Shi[1], Zhenisbek Tagay[1], Youzhe Chen[1], Lei Chen[2], Eun Sang Choi[3], Marcelo Jaime[4,+], Minseong Lee[4], Yiqing Hao[5], Huibo Cao[5], Barry L. Winn[5], Andrey A. Podlesnyak[5], Daniel M. Pajerowski[5], Ruidan Zhong[6,7,@], Xianghan Xu[7], N. P. Armitage[1], Robert Cava[7], and Collin Broholm[1,8,9,@]

[1]William H. Miller III Department of Physics and Astronomy, Johns Hopkins University, Baltimore, Maryland, USA.
[2]Department of Physics and Astronomy, Rice University, Houston, Texas, USA.
[3]National High Magnetic Field Laboratory and Department of Physics, Florida State University, Tallahassee, Florida, USA
[4]National High Magnetic Field Laboratory, Los Alamos National Laboratory, Los Alamos, New Mexico, USA.
[5]Neutron Scattering Division, Oak Ridge National Laboratory, Oak Ridge, Tennessee, USA.
[6]Tsung-Dao Lee Institute and School of Physics and Astronomy, Shanghai Jiao Tong University, Shanghai, China.
[7]Department of Chemistry, Princeton University, Princeton, New Jersey, USA.
[8]NIST Center for Neutron Research, Gaithersburg, Maryland, USA.
[9]Department of Materials Science and Engineering, Johns Hopkins University, Baltimore, Maryland, USA.
[+]New address: Physikalisch-Technische Bundesanstalt, Braunschweig, Germany
[*]These authors contributed equally: Tong Chen, Alireza Ghasemi.
[@]e-mail: tchen115@jhu.edu, rzhong@sjtu.edu.cn, broholm@jhu.edu

ABSTRACT

Supersolid phases are quantum-entangled states of matter exhibiting the dual characteristics of superfluidity and solidity. Theory predicts that hard-core bosons on a triangular lattice can form such phases at half filling and near complete filling. Leveraging an exact mapping between bosons and spin-$\frac{1}{2}$ degrees of freedom, here we show that these phases are realized in the triangular-lattice antiferromagnet $K_2Co(SeO_3)_2$. At zero field, neutron diffraction reveals the development of quasi-two-dimensional $\sqrt{3}\times\sqrt{3}$ magnetic order with Z_3 translational symmetry breaking (solidity), though with reduced amplitude indicating strong quantum fluctuations. These fluctuations manifest as equidistant bands of continuum neutron scattering, where the lowest-energy mode is gapless at K $(\frac{1}{3}\,\frac{1}{3})$, consistent with broken $U(1)$ spin rotational symmetry (superfluidity). For **c**-axis-oriented magnetic fields near saturation, we find a second phase consistent with a high-field supersolid. These two supersolids are separated by a pronounced 1/3 magnetization plateau phase that supports coherent spin waves, from which we determine the underlying spin Hamiltonian.

Introduction

Frustrated magnets can host exotic states of matter as the macroscopic degeneracies resulting from competing interactions are lifted by quantum fluctuations. In three dimensions, for example, Ising spins with ferromagnetic nearest-neighbor interactions on the pyrochlore lattice of corner-sharing tetrahedra form a degenerate "spin ice" manifold with a residual Pauling entropy $S(T=0)\approx\frac{1}{2}\log(\frac{3}{2})R\approx 0.203R$.[1,2] Theory indicates that from this manifold, quantum fluctuations can generate a quantum spin ice phase with quasi-particles sourcing the fields of emergent electromagnetism.[3–5]

In two dimensions, Ising spins with antiferromagnetic interactions on a triangular lattice form a degenerate manifold with an entropy of $S(0)=0.323R$ determined by Wannier.[6] Recent theoretical work indicates that adding quantum fluctuations to this manifold can produce a supersolid[7–10] where superfluidity and solidity coexist.[11–14] Originally studied in the context of solid ^{4}He,[15,16] the concept of supersolidity has been extended to ultracold gases[17,18] and triangular lattices of hard-core bosons,[19–23] which map to the spin-$\frac{1}{2}$ Ising model with $|\pm\frac{1}{2}\rangle$ spin states representing the presence and absence of a boson, respectively (see Methods).

The experimental realization of emergent quantum many-body phases like these in frustrated magnets must contend with subleading interactions[24] and chemical disorder,[25] which inevitably rival thermal[26,27] and quantum fluctuations in lifting degeneracies. Suitable model systems are further constrained by the availability of spectroscopic tools with sufficient resolution and sensitivity[28] to characterize the emergent phases.[29] To date, candidate materials for quantum spin ice are based on tri-valent

magnetic rare-earth elements[30] where dominant interactions are on the order of 1 K, leading to emergent energy scales in the mK range. This approaches the limits of instrumental resolution and precludes detailed experimental exploration of the emergent properties, though evidence for a π-flux quantum spin ice phase in $Ce_2Zr_2O_7$ is mounting.[31,32]

In contrast, hexagonal di-valent transition metal oxides can form quasi-two-dimensional magnets with an order of magnitude stronger interactions. Just as emergent properties of one-dimensional quantum magnets – including the gapless spinon continuum of the spin-$\frac{1}{2}$ chain[33–35] and the Haldane valence bond solid[36,37] – were characterized in transition-metal-based magnets using inelastic neutron scattering, hexagonal oxides with well-separated layers of transition metal ions that carry a spin-orbital magnetic moment,[38] provide a promising platform to explore the effects of quantum fluctuations on Wannier's manifold and to search for the predicted supersolids.

Recent work on $Na_2BaCo(PO_4)_2$ has drawn attention to this area. However, while beneficial for cryogenic applications,[39] the weak superexchange interactions mediated by the tetrahedral polyanion PO_4[40] preclude detailed neutron spectroscopy. In addition, the interlayer interactions are strong enough to induce conventional magnetic order before the emergent phase is fully developed.[41] Indeed, it now appears that the continuum scattering in $Na_2BaCo(PO_4)_2$ is actually heterogeneous spin wave scattering resulting from the incommensurate inter-plane order.[42] The situation is more favorable in $K_2Co(SeO_3)_2$ (KCSO), where the triangular lattice of spin-$\frac{1}{2}$ Co^{2+} is built around the SeO_3 polyanion that mediates an order of magnitude stronger and more anisotropic interactions within the triangular lattice planes.[43] The absence of a sharp thermal anomaly in the zero-field specific heat capacity $C_p(T)$ down to the mK regime indicates a highly two-dimensional spin system.

In this work, we explore the emergent properties of KCSO through heat capacity, magnetization, and neutron scattering experiments. We show that it is accurately described by the following spin Hamiltonian

$$\mathscr{H} = \sum_{\langle i,j \rangle} [J_z S_i^z S_j^z + J_\perp (S_i^x S_j^x + S_i^y S_j^y)] - g_z \mu_B \mu_0 H_z \sum_i S_i^z. \quad (1)$$

The first sum is over nearest neighbors on a triangular lattice, $J_z = 2.96(2)$ meV and $J_\perp = 0.21(3)$ meV, S_k^α is a spin-$\frac{1}{2}$ operator, and the second sum is the Zeeman term with $g_z = 7.8$. In zero field we observe quasi-2D $\sqrt{3} \times \sqrt{3}$ antiferromagnetic correlations below 15 K. For $T = 0.1$ K, the 44(5)% reduced root mean squared (RMS) ordered moment and the lack of ferromagnetic correlations over a similar length scale indicate quantum fluctuations. These take the form of four separate, bounded continua with roton-like minima in the lowest energy band signaling competing instabilities. At $T = 0.29$ K, the coexistence of a Goldstone mode and a pseudo-Goldstone mode at 0.060(4) meV signals the breaking of $U(1)$ rotational symmetry and Z_3 translational symmetry – the defining characteristics of a supersolid. By mapping the field-temperature phase diagram, we identify a phase transition into a 1/3 magnetization plateau belonging to the two-dimensional (2D) 3-state Potts universality class. We also present experimental evidence for a distinct high-field phase immediately below full saturation, consistent with a second theoretically predicted supersolid phase.

Results

Magnetic Order

We start by investigating static magnetism in KCSO through elastic magnetic neutron scattering. Fig. 1a-c show background-subtracted data acquired at $T = 0.1$ K in the $(hk0)$, (hhl), and $(k\bar{k}l)$ reciprocal lattice planes under 0 T and 7 T magnetic fields applied along the **c**-axis ($\mathbf{H} \parallel \mathbf{c}$). In zero field, despite the absence of sharp peaks in $C_p(T)$ data,[43] elastic scattering is sharply concentrated at the K points $(\frac{1}{3}\frac{1}{3})$ of the 2D Brillouin zone (Fig. 1a) and exhibits a rod-like character in the (hhl) plane (Fig. 1b). This indicates quasi-2D $\sqrt{3} \times \sqrt{3}$ magnetic order. The absence of scattering at the Γ points reveals that the dipole moment of each layer vanishes within the correlation volume defined by the $(\frac{1}{3}\frac{1}{3})$ rod. In a 7 T field, the intensity of the $(\frac{1}{3}\frac{1}{3})$ rod scattering is enhanced, and 3D Bragg peaks develop at the Γ points (Fig. 1a,c). This indicates Up-Up-Down (UUD) type ferrimagnetic order, in which the triangular lattice planes share a uniform magnetization but otherwise remain uncorrelated with each other.

We probe the anisotropy of the magnetic order at zero field by measuring the intensity distribution of magnetic neutron scattering versus wave vector transfer $Q_z = \mathbf{Q} \cdot \hat{\mathbf{c}} = \ell c^*$ along the rod. Fig. 1d shows the intensity decreases monotonically with ℓ for $\mathbf{Q} = (\frac{1}{3}\frac{1}{3}\ell)$ and $(\frac{2}{3}\frac{2}{3}\ell)$, with a gentle superimposed modulation that signals weak inter-layer correlations. Since the polarization factor in the magnetic neutron scattering cross section extinguishes magnetic scattering for moment $\mathbf{m} \parallel \mathbf{Q}$, the observed intensity distribution indicates the quasi-2D spin order is predominantly polarized along **c**. For comparison, an in-plane spin configuration would produce the intensity distribution shown as a dashed line in Fig. 1d.

Simultaneous fits of the $(\frac{1}{3}\frac{1}{3}l)$ and $(\frac{2}{3}\frac{2}{3}l)$ data at 0.3 K yield the solid lines in Fig. 1d with weak inter-plane correlations given by $\alpha = 0.049(7)$ and $m_\perp/m_z = 0.0(1)$ (Eq. 5). For comparison, a theoretical calculation for $J_z/J_\perp = 8$ at $T = 0$ using DMRG[7] yields $m_\perp/m_z = 0.27(g_\perp/g_z) = 0.24$, where g-factor anisotropy was obtained from high-T susceptibility data.[43] For KCSO where $J_z/J_\perp = 14$, a smaller value of $m_\perp$ is anticipated, which may explain the lack of experimental evidence for a transverse staggered magnetization. Alternatively, it could be that $m_\perp$ only develops for $T < 0.3$ K.

Since $m_\perp$ is indistinguishable from zero at 0.3 K, we can describe the spin structure in terms of Fig. 1g or Fig. 1h, which are indistinguishable based on the data in Fig. 1d. The inferred z-oriented moments on the three sites of the $\sqrt{3}\times\sqrt{3}$ unit cell are $m_z^{(g)}(1,-\frac{1}{2},-\frac{1}{2})$ with $m_z^{(g)}=3.1(3)\ \mu_B$ or $m_z^{(h)}(1,-1,0)$ with $m_z^{(h)}=2.7(3)\ \mu_B$, respectively. For both structures we obtain the root mean squared (RMS) ordered moment in the cell, $\sqrt{\overline{\langle m\rangle^2}}=\frac{1}{\sqrt{2}}m_z^{(g)}=\sqrt{\frac{2}{3}}m_z^{(h)}=2.2\ \mu_B$. Compared to the saturation magnetization for Co^{2+} of 3.90 μ_B, this corresponds to a 44(5)% reduction in the RMS ordered moment and a strongly quantum fluctuating state. Beyond these quantitative measures, having sharp rods of scattering at $\mathbf{Q}_{2D}=(\frac{1}{3}\frac{1}{3})$ but not at the Γ points (Fig. 1a,b) and no diffuse elastic scattering for $k_BT\ll J_z$ indicates a quantum fluctuating state.

Let us now examine how this state develops from the paramagnetic phase upon cooling. The $\mathbf{Q}$-integrated intensity along $(\frac{1}{3}\frac{1}{3}\ell)$ for $|\ell|\le 0.4$ – a measure of the quasi-static staggered magnetization squared $m_z(T)^2$ – and the in-plane magnetic correlation length, $\xi(T)$, are shown as functions of temperature in zero field in Fig. 1e (see also Supplementary Information (SI)). Upon cooling from 15 K to 5 K, both quantities increase. However, as $\xi(T)$ increases precipitously for $T<5$ K, the integrated intensity decreases slightly. This may indicate enhanced quantum fluctuations or enhanced inter-plane spin correlations that shift intensity from $l=0$ to larger $|l|$ that fall outside the $|\ell|\le 0.4$ integration range that the experiment probes.

Phase Diagram

We now explore the $H-T$ phase diagram for magnetic field applied along the **c**-axis. Fig. 2a shows the heat capacity, $C_p(T)$, for $\mu_0H=14$ T. While the zero-field data exhibit a broad peak centered around 1.0 K, at higher fields, sharp peaks indicating a second-order phase transition emerge. These become more pronounced and shift to higher temperatures with increasing field, eventually reaching a maximum transition temperature of 11.4 K for $\mu_0H=10$ T. Neutron diffraction (Fig. 1a,c) indicates that for fields above 2 T, this phase boundary separates the $\sqrt{3}\times\sqrt{3}$ periodic UUD and paramagnetic phases. The phase boundary is, thus, associated with breaking Z_3 sublattice symmetry as a D sublattice is spontaneously selected from three. For both classical[44] and quantum Ising models on a triangular lattice,[9,10] this transition is predicted to be in the 2D three-state Potts universality class. Fitting the critical regime to $C_p(T)\propto 1/(T-T_c(H))^\alpha$ yields $\alpha=0.318(3)$ (details in SI), which is consistent with the exact theoretical value of $\alpha=\frac{1}{3}$.[45]

Fig. 2b and 2c show the uniform magnetization, $M(T)$, and differential susceptibility, dM/dT, for DC fields up to 30 T. Upon cooling in fields between 2 T and 17 T, the magnetization approaches 1/3 of the 3.90 μ_B/Co saturation value, which also indicates the UUD state. For fields beyond 22 T, the magnetization approaches saturation. The resulting $H-T$ phase diagram derived from dM/dT (Fig. 2c) reveals a pronounced UUD phase, consistent with the classical Ising model ($J_\perp=0$) on a triangular lattice.[46,47] In the boson representation, this corresponds to a honeycomb lattice of bosons filling 2/3 of the triangular lattice sites. Direct comparison between the measured and calculated phase diagrams yields $J_z\approx 3.0$ meV.

Using a Maxwell relation (see Methods), we obtain the field and temperature dependence of the magnetic entropy $\Delta S_m(T,H)/R\ln 2$ from the magnetization data as shown in Fig. 2d. The blue regions, where $\Delta S_m\approx 0$, distinguish gapped long-range ordered phases. Conversely, the regions where ΔS_m remains large to low temperatures indicate emergent gapless phases. For fields between 17 T and 21 T, an additional phase emerges, evidenced by a double-peak structure in the dM/dT data versus temperature (Fig. 2c inset). This observation aligns with theoretical predictions of a high-field supersolid phase from cluster mean-field and DMRG studies of Eq. 1 with $J_\perp<J_z$.[9,10] Comparing the $T\to 0$ phase boundaries (μ_0H_{c1} and μ_0H_{c2} in Fig. 2c,d) with these numerical studies[9,10] indicates $J_\perp\approx 0.23$ meV. Occurring near full magnetization, which is near full occupancy in the boson language, this high-field supersolid phase is also predicted to break both Z_3 and $U(1)$ symmetries. The lower boundary of the high-field supersolid phase is predicted to be first-order for spin-$\frac{1}{2}$ quantum Ising magnets ($J_\perp<0.4J_z$) in numerical work.[9,10] This is consistent with the steep jump observed in the $M(T)$ (Fig. 2b), and is one of the key features that distinguish KCSO from $Na_2BaCo(PO_4)_2$.[48,49] From Fig. 2d, we estimate the change in entropy across the phase transition from the UUD phase to the putative supersolid $\Delta S_m=0.4(1)R\ln 2$ from which the Clausius-Clapeyron relation yields the slope of the phase boundary $\mu_0dH_c/dT_c=-\Delta S_m/\Delta M=-0.5(1)$ T/K, which is consistent with the slope of $-0.51(1)$ T/K inferred from Fig. 2c.

To explore the low-field and low-temperature region of the phase diagram, we examine the magnetic field dependence of M, dM/dH, and C_p in Fig. 3. The $H\to 0$ differential susceptibility dM/dH continuously increases upon cooling to the lowest temperatures accessed (0.3 K), indicating gapless magnetic excitations at low fields (Fig. 3a,b). In fact, at the lowest H and T, dM/dH increases with field, leading to a peak at an apparent crossover field that approaches 0.51(3) T at low T. Considering that Z_3 symmetry is broken in the UUD phase, the fact that this phase can be accessed through a crossover at the lowest temperature indicates that Z_3 symmetry is effectively broken in zero field at these temperatures. This is consistent with the long correlation length ξ of the UUD phase (Fig. 1e). Fig. 3c,d show the apparent termination of the Potts transition at (T, μ_0H) = (4.5 K, 1.1 T), which may represent the vanishing of entropy associated with the transition rather than a critical endpoint. This would be consistent with the theoretical predictions of successive Berezinskii–Kosterlitz–Thouless (BKT) transitions associated with Z_3 symmetry breaking[50–53] extending from this point to zero field (Fig. 3e).

For temperatures above 5 K, where the crossover peak in dM/dH is absent, M increases linearly with H (Fig. 3a) at low fields, and the transition to the UUD phase is marked by a sharp peak (Fig. 3b), consistent with the Potts transition. With increasing temperature, this Potts transition peak gains strength and shifts to higher fields (Fig. 3c). At 10 K, the re-entrant nature of the UUD phase is apparent, with a second sharp peak marking the upper boundary of the UUD phase within the accessible 14 T field range. Note that the putative high-field supersolid phase, identified from dM/dT (Fig. 2c), is not yet apparent in this field regime.

Coherent Spin-Waves in the UUD Phase

A direct comparison between experiments and theory requires accurate knowledge of the underlying spin Hamiltonian. We obtain this through measurements of inelastic magnetic neutron scattering in the UUD phase at 7 T, where the magnetic scattering cross section can be calculated from the spin Hamiltonian using linear spin-wave theory. Displayed in Fig. 4, the scattering data reveal three coherent spin-wave modes, consistent with the long-range ordered $\sqrt{3}\times\sqrt{3}$ UUD state. The absence of measurable dispersion along the **c**-axis ($M_1 \rightarrow L_1$ in Fig. 4a), along with the rod-like nature of the magnetic diffraction in Fig. 1c, provides clear evidence of a quasi-2D spin system.

We attribute the highest energy excitation in Fig. 4a to the flipping of a D spin, which is surrounded by $z = 6$ U spins in the UUD phase. While spin-wave propagation is driven by $J_\perp$ (Eq. 1) through the reversal of an anti-parallel spin pair, no such spin-flip process is possible after flipping an isolated D spin, which explains the dispersionless nature of the minority spin-flip excitation. The energy cost of this spin flip is approximately $2zJ_zS^2 - 2g_zS\mu_B\mu_0H \approx 5.84$ meV, in good agreement with the experiment (Fig. 4a). Here, $J_z \approx 3.0$ meV and $g_z = 7.8$ were inferred from the $H-T$ phase diagram and the saturation magnetization, respectively. The two lower-energy dispersive modes in the 7 T data are each associated with flipping one of the two U spins in the unit cell. Since U spins are surrounded by an equal number of U and D spins, the **Q**-averaged energy for these modes is simply $2g_zS\mu_B\mu_0H = 3.16$ meV. Dispersion arises because the newly created D spin can move to adjacent U sites via the transverse exchange term, and the bandwidth of these lower branches in Fig. 4a provides an estimate of $3J_\perp \approx 0.69$ meV.

The assignment of the upper mode to $\Delta S_z = +1$ (D $\rightarrow$ U) and the lower modes to $\Delta S_z = -1$ (U $\rightarrow$ D) is consistent with the observation that the bands move towards each other with increasing field (see Fig. S14 and S15). As the applied field increases, the energy of the spin-flip excitation (D $\rightarrow$ U) decreases and eventually softens to zero, leading to the condensation of the upper, nearly dispersionless spin-wave mode at $\mu_0H_{c1}^{calc} = 6J_zS/g_z\mu_B \approx 19.9$ T. At still higher fields, the ferromagnetic spin wave in the fully polarized phase condenses at $\mu_0H_{c2}^{calc} = 3(2J_z+J_\perp)S/g_z\mu_B \approx 20.7$ T.[49] The separation between the two critical fields $\mu_0H_{c1}^{calc}$ and $\mu_0H_{c2}^{calc}$ accounts for the experimentally observed intermediate phase between the UUD and field-polarized regimes (Fig. 2c,d). Numerical studies of the spin-$\frac{1}{2}$ XXZ model on the triangular lattice[9,10] identify this intermediate region as a high-field supersolid phase. While the upper critical field $\mu_0H_{c2}^{calc}$ is exact at $T = 0$, the lower boundary $\mu_0H_{c1}^{calc}$ is predicted to become a first-order transition in quantum Ising magnets with $J_\perp < 0.4J_z$.

To extract the most accurate values for the exchange constants, we performed a pixel-to-pixel least squares fit of linear spin-wave theory, as implemented in SpinW,[54] to the data in Fig. 4a. The calculated spin-wave cross section was convoluted with a Gaussian energy resolution with a full width at half maximum (FWHM) of 0.2 meV. Given the weak dispersion, effects of the finite instrumental **Q**-resolution are negligible. As shown in Fig. 4b, an excellent account of the data is achieved with $J_z = 2.96(2)$ meV and $J_\perp = 0.21(3)$ meV. By including the next-nearest-neighbor interactions in the spin-wave calculation and comparing the resulting scattering cross section to the data, we obtained a stringent constraint on such interactions: $J_z^{(2)} = 0.02(4)$ meV and $J_\perp^{(2)} = 0.00(5)$ meV. The dominance of nearest-neighbor interactions is essential for exploring supersolid phases, as longer-range interactions can stabilize alternative ground states.[55] The sharp spin-wave modes in Fig. 4 also highlight the high quality of our multi-crystal sample and allow us to focus on intrinsic, as opposed to disorder-based, interpretations of the low-field continuum scattering.

Magnetic Excitations in Zero Field

Let us now examine the magnetic excitation spectrum in the low-T, low-H limit. Though the correlation length for $\sqrt{3}\times\sqrt{3}$ quasi-static spin correlations exceeds $\xi > 200\,a$, where a is the in-plane lattice constant, the fact that the RMS ordered moment is reduced by as much as $44(5)\%$ compared to the 7 T UUD phase indicates strong quantum fluctuations are present. Fig. 5a shows the energy and momentum dependence of these fluctuations at 0.1 K. The data reveal three distinct bands of magnetic scattering near 0 meV, 3 meV, and 6 meV. These bands exhibit some **Q**-dependent structure (Fig. 5b,c) and are broader than the instrumental energy resolution. A fourth band at 8.9(1) meV is inferred from THz spectroscopy (see Fig. S15 and S16 in SI).

To understand these bands, we first consider the classical Ising model without transverse exchange ($J_\perp = 0$). In this limit, magnetic excitations are individual spin-flips within the exchange field generated by the six nearest neighbors. The cost of a spin-flip is $\hbar\omega_n = J_z\Delta S^z\langle\sum_i S_i^z\rangle = J_z\langle S_{tot}^z\rangle = n\times J_z$, where $n = 0,1,2,3$ correspond to the four quantized values of the Ising exchange field.[56,57] Since a long-range ordered UUD state would only exhibits excitations corresponding to $n = 0$ (for U sites) and $n = 3$ (for D sites), our observation of four bands of excitations in the low-T and low-H limit indicates that in KCSO

quantum fluctuations driven by $J_\perp$ ensure that all four possible values of the exchange-field occur (Fig. 5a). The broadening of the bands and the near-neighbor antiferromagnetic correlations indicated by the suppression of intensity at Γ-points (Fig. 5b,c) are also a result of $J_\perp$.

Focusing on the lowest energy band of scattering at $T = 0.29$ K, the higher-resolution data in Fig. 5d-f show that it consists of a diffusive continuum with quasi-particle-like accumulation of intensity along its lower edge, which is consistent with a very recent study[58]. The strongest intensity and the lowest energy modes are found at the ordering wave vector, K. Consistent with the magnetization (Fig. 3a) and specific heat capacity data (Fig. 3e), the spectrum is gapless at K but also includes a finite-energy peak (Fig. 6). The gapless and gapped excitations can be modeled as over- and under-damped harmonic oscillators, respectively, with the following dynamic correlation function

$$S(\mathbf{Q},\omega) = (1+n(\omega))\frac{1}{\hbar}\left[\frac{\chi_0\Gamma_{\rm QE}\omega}{\Gamma_{\rm QE}^2+\omega^2} + \frac{A}{\pi}\left(\frac{\Gamma_{\rm DHO}}{(\omega-\omega_0)^2+\Gamma_{\rm DHO}^2} - \frac{\Gamma_{\rm DHO}}{(\omega+\omega_0)^2+\Gamma_{\rm DHO}^2}\right)\right]. \quad (2)$$

Here $n(\omega) = (\exp(\hbar\omega/k_BT)-1)^{-1}$ is the Bose-Einstein population factor. The optimal fit to the constant-$\mathbf{Q}$ cut (Fig. 6b,c) yields a relaxation rate of $\hbar\Gamma_{\rm QE} = 7(2)$ μeV for the quasi-elastic component, and a damping rate of $\Gamma_{\rm DHO} = 29(8)$ μeV with a gap $\hbar\omega_0 = 60(4)$ μeV for the finite energy mode. The plot of χ^2 versus the parameters of the quasi-elastic component in the inset to Fig. 6c shows that both components are needed to describe the measured spectrum. In particular the instrumental energy resolution measured through nuclear incoherent elastic scattering scaled to the intensity of the truly elastic magnetic component (open circles in Fig. 6c) is sharper than the quasi-elastic component in the data for positive and negative $\hbar\omega$. The ratio of spectral weights in the three components over the accessible energy range is $I_{\rm E} : I_{\rm QE} : I_{\rm DHO} = 1 : 0.023(6) : 0.071(5)$. The gap of the finite energy mode is found to collapse as the translational periodicity of the triangular lattice is restored by warming (see Fig. S13 in SI for details). These data are consistent with a supersolid phase wherein the truly elastic component $I_{\rm E}$ represents the frozen $\sqrt{3}\times\sqrt{3}$ Y-order, $I_{\rm QE}$ would be the gapless Goldstone mode associated with $U(1)$ rotational symmetry breaking,[59,60] and $I_{\rm DHO}$ would be a pseudo Goldstone mode resulting from the order-by-disorder mechanism[61] in the presence of quasi-long-range $\sqrt{3}\times\sqrt{3}$ order.[62] However, other viable interpretations exist including that I_{QE} could be gapless critical scattering associated with a thermal or quantum phase transition to a gapped phase.

At progressively higher energies, Fig. 5d shows local spectral minima at M and at $\frac{1}{2}$K. Beyond the maximum in the dispersive lower-edge mode, there is clear evidence for continuum scattering extending to approximately 0.6 meV. All of these features can be appreciated in the $\mathbf{Q}$-dependence of constant-energy slices through the same data in Fig. 5e,f. Note that this entire spectrum is generated by quantum fluctuations and is wholly inaccessible to conventional spin wave theory. This includes the finite energy minima at M and $\frac{1}{2}$K, which, recalling the roton minimum in superfluid ^{4}He, indicate proximate phases that might be stabilized with suitable additional interactions. We note that the spin wave data in (Fig. 4a) place strict limits on further neighbor interactions. The higher-energy continuum of excitations recalls the two-spinon scattering cross section for spin-$\frac{1}{2}$ chain materials,[33–35] suggesting that the supersolid phase might be viewed as a precursory quantum spin liquid.[63]

Discussion

$K_2Co(SeO_3)_2$ has proven to be an excellent platform for exploring the emergent properties of a foundational model in frustrated magnetism. In contrast to quantum spin ice, for which only rare-earth model systems are available, this $Co^{2+}(3d^7)$ based triangular-lattice system provides unprecedented experimental access to the rich emergent properties that can arise when quantum fluctuations lift the degeneracy of a frustrated spin manifold. Furthermore, a simple state – the field-induced long-range UUD three-sublattice ordered phase – is accessible to inelastic neutron scattering, allowing the parameters in the spin-Hamiltonian (Eq. 1) to be accurately determined. In particular, the lack of dispersion of the minority spin-flip excitation provides direct experimental evidence that nearest neighbor interactions dominate. The ratio $J_z/J_\perp = 14(2)$ places KCSO deeply in the Ising limit while the magnitude of J_z ensures the emergent quantum dynamics is readily accessible to modern neutron scattering instrumentation.

Elastic neutron scattering in zero field reveals the gradual onset of solidity below 15 K, indicated by the quasi-2D $\sqrt{3}\times\sqrt{3}$ magnetic order associated with Z_3 translational symmetry breaking. The lack of scattering at the Γ points (Fig. 1a,b) and the 44(5)% reduced RMS ordered moment at 0.3 K reflect strong quantum fluctuations. The quantum fluctuations are also apparent in bands of magnetic excitations at quantized energies $\hbar\omega = n\times J_z$. At the critical K-point the coexistence of a gapless and a gapped mode at 0.29 K (Fig. 6) may be associated with the breaking of $U(1)$ spin rotational symmetry (superfluidity) and the lifting of an accidental XY degeneracy (solidity), respectively, as anticipated for a supersolid. In mapping the full $H-T$ phase diagram of KCSO, which includes a prominent UUD phase, we have also documented an additional low-T phase near full magnetization that is consistent with theoretical predictions for a second supersolid phase.

Consistent results focusing on the low-H limit and low-energy spectra have been published very recently.[58,64] While these studies provide valuable insights into the low-field regime, our work offers a significantly more comprehensive $H-T$ phase

diagram. In particular, our results reveal a second supersolid phase near magnetic saturation, a regime that has remained largely unexplored. Furthermore, our measurements push the energy resolution at the elastic line down to a FWHM of 10.3 μeV in zero field, providing the precision necessary to identify subtle spectral features of the low-field supersolid phase. Following the posting of our manuscript on arXiv, theorists have begun using advanced numerical methods to simulate these experimental results[65–69], further highlighting the role of $K_2Co(SeO_3)_2$ as a benchmark model system.

Methods

Hard-Core Boson Representation

The quantum magnetic order emerging in spin-$\frac{1}{2}$ systems on a triangular lattice, as described by the spin-Hamiltonian in Equation(1), can be conveniently understood by representing the spin operators with hard-core bosons

$$S_i^z = n_i - \frac{1}{2}, \quad S_i^+ = \quad b_i^\dagger, \quad S_i^- = b_i, \tag{3}$$

where $n_i = b_i^\dagger b_i$ is restricted to 0 or 1. Rewriting the Hamiltonian (Eq.(1)) in terms of the hard-core bosons yields:

$$\mathscr{H} = \sum_{\langle i,j \rangle} \left[V \left(n_i - \frac{1}{2} \right) \left(n_j - \frac{1}{2} \right) - t(b_i^\dagger b_j + b_j^\dagger b_i) \right] - \mu \sum_i \left(n_i - \frac{1}{2} \right), \tag{4}$$

where the model parameters are $V = J_z$, $-t = \frac{1}{2} J_\perp$ and $\mu = g_z \mu_B \mu_0 H_z$. In this bosonic representation, $V > 0$ signifies a repulsive interaction between nearest-neighbor bosons, $-t$ represents the hopping amplitude, and μ corresponds to the chemical potential. The rotational symmetry of the x- and y-components of the spins becomes $U(1)$ symmetry of the bosons.

We focus on two distinct types of orders: diagonal density order and off-diagonal phase order. Diagonal order corresponds to charge density waves (or equivalently, spatial modulations in $\langle S^z \rangle$) and is often referred to as solidity. Off-diagonal order involves the spontaneous breaking of the $U(1)$ symmetry and is characteristic of superfluidity. According to the Mermin-Wagner theorem, true long-range order associated with a continuous symmetry cannot develop at finite temperatures in a 2D system. In the superfluid phase that exhibits a quasi-long-range order, the correlation length is limited by thermally generated bound vortex–antivortex pairs.

The antiferromagnetic Heisenberg model on triangular lattices with easy-axis anisotropy has been suggested to host phases exhibiting both diagonal and off-diagonal long-range order, referred to as supersolids. Since $m_\perp = g_\perp \langle S_\perp \rangle$ is linked to the creation and annihilation of bosons ($b^\dagger$ and b), a nonzero $m_\perp$ reflects a macroscopic quantum coherence of the bosons, which is indicative of superfluidity. Similarly, a nonzero $m_z = g_z \langle S_z \rangle$ reflects the spatial modulation of boson density, which is analogous to a classical charge density wave in a solid.

Materials Synthesis

$K_2Co(SeO_3)_2$ single crystals were synthesized using a previously reported solid-state reaction method at Johns Hopkins University and Princeton University[43]. Dried K_2CO_3 (99%), CoO (99%), and Se_O2 (99%) were mixed in a 1.2:1:2.2 molar ratio. The mixture was loaded into an alumina crucible and subsequently sealed in a quartz tube under vacuum. The assembly was heated at 600 °C for 8 hours and then slowly cooled down to room temperature in 8 hours. Neither stacking faults nor secondary phases were detected in X-ray diffraction analysis of polycrystalline samples. The crystals were found to crystallize in the space group $R\bar{3}m$ (No. 166) with lattice constants $a = b = 5.5049(7)$ Å, and $c = 18.411(3)$ Å at 100 K.

Specific Heat

The specific heat capacity of KCSO was measured using a thermal-relaxation method in a Quantum Design Physical Properties Measurement System (PPMS) at Johns Hopkins University. A 2.1 mg plate-like sample was mounted with its primary face horizontal to align the **c**-axis with the vertical field direction of the 14 T magnet.

Magnetization

High-field DC magnetization data up to 30 T, $M(T)$, were obtained at the National High Magnetic Field Laboratory (NHMFL) in Tallahassee, Florida. The measurements used a conventional vibrating sample magnetometer (VSM) in a water-cooled resistive magnet located in Cell 8 of the DC Field Facility. The VSM was calibrated using a standard Ni sphere, and the sample was glued to a polycarbonate sample holder with GE7031 varnish. The magnetization data were normalized against DC magnetization measurements performed with a VSM in a 14 T PPMS (Quantum Design) at Johns Hopkins University.

From the Maxwell relation $(\partial S/\partial H)_T = \mu_0 (\partial M/\partial T)_H$, we can derive the isothermal change in entropy $\Delta S_m(H) = \mu_0 \int_0^H (\partial M/\partial T)_{H'} \mathrm{d}H'$.[70] By combining this with the change in entropy $\Delta S_m(T, H = 0)$ inferred from zero-field specific heat capacity data, we obtain the full field and temperature dependence of the entropy $\Delta S_m(T,H)/R \ln 2$.

The magnetization, $M(H)$, in millisecond pulsed magnets reaching up to 60 T were measured at the NHMFL pulsed field facility at Los Alamos National Laboratory. The experiments were conducted in three configurations with magnetic fields along the **c**-axis direction. To reduce the background from the spatially uniform pulsed magnetic field, the samples were placed in a radially counter-wound copper coil. An additional one turn of the coil further compensated for any residual signals. For each temperature, two measurements were taken: one with the sample inside the coil and one with it outside. The final magnetization curve was obtained by subtracting the "sample-out" background signal from the "sample-in" data. The temperature was stabilized using a ^{3}He system, and a Lakeshore Cernox thermometer recorded the temperature before each field pulse. The pulsed-field data in Fig. S5 clearly display two high field maxima in dM/dH indicating an additional phase near magnetization saturation. The rapid magnetization and demagnetization processes resulted in considerable sample heating and cooling, respectively, consistent with suggestions to use such materials for cryogenic refrigeration.[39] For this reason, we chose to base the phase diagram in Fig. 2 on DC magnetization data only.

Elastic Neutron Scattering

Neutron diffraction experiments were conducted using the HB-3A DEMAND diffractometer[71] at the High Flux Isotope Reactor at Oak Ridge National Laboratory. An 8.22 mg single crystal was mounted on an oxygen-free high-thermal-conductivity (OFHC) copper holder and cooled using a ^{3}He insert with a base temperature of 0.3 K. The experiment used a four-circle mode and a beam of neutrons with a wavelength $\lambda = 1.542$ Å from a bent Si-220 monochromator.

Fig. 1d shows the magnetic elastic scattering versus $\mathbf{Q} = (\frac{1}{3}\frac{1}{3}l)$ and $(\frac{2}{3}\frac{2}{3}l)$, measured in zero field without final energy analysis. The broad peaks versus l indicate quasi-2D magnetic order with moments predominantly oriented along the **c**-axis. The dashed and solid lines in Fig. 1d represent calculations based on the following expression for neutron diffraction from an anisotropic quasi-2D magnetic structure with ($\alpha \neq 0$) and without ($\alpha = 0$) inter-plane correlations:

$$I(\mathbf{Q}) = N_{\mathrm{M}} \frac{(2\pi)^2}{A_{\mathrm{M}}} \left(\frac{\gamma r_0}{2}\right)^2 |F(\mathbf{Q})|^2 \times (1 + 2\alpha \cos(\frac{2\pi l}{3})) \times \Big(\underbrace{(1 - \hat{Q}_z^2)|\mathcal{F}_z(\mathbf{Q})|^2}_{\text{solidity}} + \underbrace{\frac{1}{2}(1 + \hat{Q}_z^2)|\mathcal{F}_\perp(\mathbf{Q})|^2}_{\text{superfluidity}} \Big). \tag{5}$$

This expression is based on the following approximation $\langle S_i^\alpha(t) S_j^\beta(0)\rangle \approx \langle S_i^\alpha\rangle\langle S_j^\beta\rangle$ and averaging over all domains. N_{M} and A_{M} are the number and in-plane area of magnetic unit cells; $\gamma r_0 = -0.54 \cdot 10^{-12}$ cm is the magnetic scattering length; $\mathbf{Q}$ is the momentum transfer; $(1 + 2\alpha\cos(\frac{2\pi l}{3}))$ accounts for inter-plane correlations; and $(1 - \hat{Q}_z^2)$ and $\frac{1}{2}(1 + \hat{Q}_z^2)$ are domain averaged polarization factors for the two components of the magnetic structure. $F(\mathbf{Q})$ is the magnetic form factor, which we approximate as the atomic form factor for Co^{2+}.[72]

$\mathcal{F}_{z,\perp}(\mathbf{Q}) = \sum_j m_{z,\perp}^{(j)} \exp(i\mathbf{Q}\cdot\mathbf{d}_j)$ are the scalar magnetic structure factor for the in- and out-of-plane components of the dipole moments $m_{z,\perp}^{(j)}$ at locations $\mathbf{d}_j$ within the $\sqrt{3}\times\sqrt{3}$ magnetic unit cell. For all allowed magnetic Bragg peaks of the structures in Fig. 1f-h we have $|\mathcal{F}_z^{(f,g)}|^2 = \frac{9}{4}m_z^2$, $|\mathcal{F}_\perp^{(f)}|^2 = 3m_\perp^2$, and $|\mathcal{F}_z^{(h)}|^2 = 3m_z^2$. Here $m_{z,\perp}$ denote the largest parallel and perpendicular component of the ordered dipole moment, respectively.

Inelastic Neutron Scattering

The neutron scattering data were collected on the HYSPEC and CNCS direct geometry spectrometers at Oak Ridge National Laboratory. For the HYSPEC experiment, single crystals with a total mass of 0.9 g were co-aligned on an aluminum mount for scattering in the $(hk0)$ reciprocal lattice plane. The sample was cooled in a dilution refrigerator with an 8 T vertical field magnet to a base temperature of 70 mK. Measurements used incident energies E_i =3.8 meV and 9.0 meV with a 240 Hz chopper frequency. The sample was rotated through 60° or 120° in 1° steps. In the 0.1 K "zero-field" measurement, a 0.02 T field was applied to maintain the aluminum sample mount in its thermally conductive normal state. Data were normalized against the magnetic Bragg diffraction intensity in the plateau phase, where the sublattice magnetization is known to be $m_z = 3.90\ \mu_{\mathrm{B}}$. Measurements on CNCS employed a ^{3}He insert in a cryostat with a base temperature of 0.29 K. $E_i = 0.72$ meV and 1.0 meV were used with a 300 Hz chopper frequency in high-flux mode. The sample was rotated through 30° or 60° in 1° steps. The CNCS data were normalized to the HYSPEC measurements using the incoherent elastic scattering cross section.

THz Spectroscopy

Time-domain terahertz spectroscopy measurements were performed in a home-built system equipped with a commercial fiber-coupled Toptica spectrometer and a 6.5 T superconducting magnet.[73] The magnetic field was applied along the **c**-axis. The complex THz transmission matrix was measured in a frequency range from 0.2 THz to 2 THz.

Data Availability

The numerical data underlying the magnetization, specific heat, and elastic neutron scattering figures have been deposited in the Figshare database and can be accessed at https://figshare.com/s/9771e9a4e5a2cac62fb8. Due to the large file sizes, the raw inelastic neutron scattering datasets are hosted in the ORNL database https://analysis.sns.gov under the experiment identifier IPTS-29655. Processed inelastic neutron scattering data and all other data that support the findings of this study are available from the corresponding authors upon request.

References

1. Ramirez, A. P., Hayashi, A., Cava, R. J., Siddharthan, R. & Shastry, B. Zero-point entropy in 'spin ice'. *Nature* **399**, 333–335, DOI: https://doi.org/10.1038/20619 (1999).
2. Bramwell, S. T. & Gingras, M. J. Spin ice state in frustrated magnetic pyrochlore materials. *Science* **294**, 1495–1501, DOI: https://doi.org/10.1126/science.1064761 (2001).
3. Savary, L. & Balents, L. Coulombic quantum liquids in spin-1/2 pyrochlores. *Phys. Rev. Lett.* **108**, 037202, DOI: https://doi.org/10.1103/PhysRevLett.108.037202 (2012).
4. Lee, S., Onoda, S. & Balents, L. Generic quantum spin ice. *Phys. Rev. B-Condensed Matter Mater. Phys.* **86**, 104412, DOI: https://doi.org/10.1103/PhysRevB.86.104412 (2012).
5. Gingras, M. J. & McClarty, P. A. Quantum spin ice: a search for gapless quantum spin liquids in pyrochlore magnets. *Reports on Prog. Phys.* **77**, 056501, DOI: https://doi.org/10.1088/0034-4885/77/5/056501/ (2014).
6. Wannier, G. Antiferromagnetism. The triangular Ising net. *Phys. Rev.* **79**, 357, DOI: https://doi.org/10.1103/PhysRev.79.357 (1950).
7. Jiang, H., Weng, M., Weng, Z., Sheng, D. & Balents, L. Supersolid order of frustrated hard-core bosons in a triangular lattice system. *Phys. Rev. B* **79**, 020409, DOI: https://doi.org/10.1103/PhysRevB.79.020409 (2009).
8. Heidarian, D. & Paramekanti, A. Supersolidity in the triangular lattice spin-1/2 XXZ model: A variational perspective. *Phys. Rev. Lett.* **104**, 015301, DOI: https://doi.org/10.1103/PhysRevLett.104.015301 (2010).
9. Yamamoto, D., Marmorini, G. & Danshita, I. Quantum phase diagram of the triangular-lattice XXZ model in a magnetic field. *Phys. Rev. Lett.* **112**, 127203, DOI: https://doi.org/10.1103/PhysRevLett.112.127203 (2014).
10. Sellmann, D., Zhang, X.-F., Eggert, S. *et al.* Phase diagram of the antiferromagnetic XXZ model on the triangular lattice. *Phys. Rev. B* **91**, 081104, DOI: https://doi.org/10.1103/PhysRevB.91.081104 (2015).
11. Thouless, D. The flow of a dense superfluid. *Annals Phys.* **52**, 403–427, DOI: https://doi.org/10.1016/0003-4916(69)90286-3 (1969).
12. Andreev, A. & Lifshits, I. Quantum theory of defects in crystals. *Zhur Eksper Teoret Fiziki* **56**, 2057–2068, DOI: https://doi.org/10.1070/PU1971v013n05ABEH004235 (1969).
13. Chester, G. Speculations on bose-einstein condensation and quantum crystals. *Phys. Rev. A* **2**, 256, DOI: https://doi.org/10.1103/PhysRevA.2.256 (1970).
14. Leggett, A. J. Can a solid be "superfluid"? *Phys. Rev. Lett.* **25**, 1543, DOI: https://doi.org/10.1103/PhysRevLett.25.1543 (1970).
15. Kim, E. & Chan, M. H.-W. Probable observation of a supersolid helium phase. *Nature* **427**, 225–227, DOI: https://doi.org/10.1038/nature02220 (2004).
16. Boninsegni, M. & Prokof'ev, N. V. Colloquium: Supersolids: What and where are they? *Rev. Mod. Phys.* **84**, 759, DOI: https://doi.org/10.1103/RevModPhys.84.759 (2012).
17. Li, J.-R. *et al.* A stripe phase with supersolid properties in spin–orbit-coupled bose-einstein condensates. *Nature* **543**, 91–94, DOI: https://doi.org/10.1038/nature21431 (2017).
18. Léonard, J., Morales, A., Zupancic, P., Esslinger, T. & Donner, T. Supersolid formation in a quantum gas breaking a continuous translational symmetry. *Nature* **543**, 87–90, DOI: https://doi.org/10.1038/nature21067 (2017).
19. Melko, R. *et al.* Supersolid order from disorder: Hard-core bosons on the triangular lattice. *Phys. Rev. Lett.* **95**, 127207, DOI: https://doi.org/10.1103/PhysRevLett.95.127207 (2005).
20. Wessel, S. & Troyer, M. Supersolid hard-core bosons on the triangular lattice. *Phys. Rev. Lett.* **95**, 127205, DOI: https://doi.org/10.1103/PhysRevLett.95.127205 (2005).

21. Boninsegni, M. & Prokof'ev, N. Supersolid phase of hard-core bosons on a triangular lattice. *Phys. Rev. Lett.* **95**, 237204, DOI: https://doi.org/10.1103/PhysRevLett.95.237204 (2005).

22. Heidarian, D. & Damle, K. Persistent supersolid phase of hard-core bosons on the triangular lattice. *Phys. Rev. Lett.* **95**, 127206, DOI: https://doi.org/10.1103/PhysRevLett.95.127206 (2005).

23. Wang, F., Pollmann, F. & Vishwanath, A. Extended supersolid phase of frustrated hard-core bosons on a triangular lattice. *Phys. Rev. Lett.* **102**, 017203, DOI: https://doi.org/10.1103/PhysRevLett.102.017203 (2009).

24. den Hertog, B. C. & Gingras, M. J. Dipolar interactions and origin of spin ice in ising pyrochlore magnets. *Phys. Rev. Lett.* **84**, 3430, DOI: https://doi.org/10.1103/PhysRevLett.84.3430 (2000).

25. Syzranov, S. & Ramirez, A. Eminuscent phase in frustrated magnets: a challenge to quantum spin liquids. *Nat. Commun.* **13**, 2993, DOI: https://doi.org/10.1038/s41467-022-30739-0 (2022).

26. Villain, J., Bidaux, R., Carton, J.-P. & Conte, R. Order as an effect of disorder. *J. de Physique* **41**, 1263–1272, DOI: https://doi.org/10.1051/jphys:0198000410110126300 (1980).

27. Henley, C. L. Ordering due to disorder in a frustrated vector antiferromagnet. *Phys. Rev. Lett.* **62**, 2056, DOI: https://doi.org/10.1103/PhysRevLett.62.2056 (1989).

28. Stone, M. B. *et al.* A comparison of four direct geometry time-of-flight spectrometers at the spallation neutron source. *Rev. Sci. Instruments* **85**, DOI: https://doi.org/10.1063/1.4870050 (2014).

29. Chamorro, J. R., McQueen, T. M. & Tran, T. T. Chemistry of quantum spin liquids. *Chem. Rev.* **121**, 2898–2934, DOI: https://doi.org/10.1021/acs.chemrev.0c00641 (2020).

30. Gardner, J. S., Gingras, M. J. & Greedan, J. E. Magnetic pyrochlore oxides. *Rev. Mod. Phys.* **82**, 53–107, DOI: https://doi.org/10.1103/RevModPhys.82.53 (2010).

31. Gao, B. *et al.* Experimental signatures of a three-dimensional quantum spin liquid in effective spin-1/2 $Ce_2Zr_2O_7$ pyrochlore. *Nat. Phys.* **15**, 1052–1057, DOI: https://doi.org/10.1038/s41567-019-0577-6 (2019).

32. Gaudet, J. *et al.* Quantum spin ice dynamics in the dipole-octupole pyrochlore magnet $Ce_2Zr_2O_7$. *Phys. Rev. Lett.* **122**, 187201, DOI: https://doi.org/10.1103/PhysRevLett.122.187201 (2019).

33. Tennant, D., Perring, T., Cowley, R. & Nagler, S. Unbound spinons in the S= 1/2 antiferromagnetic chain $KCuF_3$. *Phys. Rev. Lett.* **70**, 4003, DOI: https://doi.org/10.1103/PhysRevLett.70.4003 (1993).

34. Lake, B., Tennant, D. A., Frost, C. D. & Nagler, S. E. Quantum criticality and universal scaling of a quantum antiferromagnet. *Nat. Mater.* **4**, 329–334, DOI: https://doi.org/10.1038/nmat1327 (2005).

35. Mourigal, M. *et al.* Fractional spinon excitations in the quantum heisenberg antiferromagnetic chain. *Nat. Phys.* **9**, 435–441, DOI: https://doi.org/10.1038/nphys2652 (2013).

36. Ma, S., Broholm, C., Reich, D. H., Sternlieb, B. & Erwin, R. Dominance of long-lived excitations in the antiferromagnetic spin-1 chain NENP. *Phys. Rev. Lett.* **69**, 3571, DOI: https://doi.org/10.1103/PhysRevLett.69.3571 (1992).

37. Zaliznyak, I., Lee, S.-H. & Petrov, S. Continuum in the spin-excitation spectrum of a haldane chain observed by neutron scattering in $CsNiCl_3$. *Phys. Rev. Lett.* **87**, 017202, DOI: https://doi.org/10.1103/PhysRevLett.87.017202 (2001).

38. Liu, X. & Kee, H.-Y. Non-Kitaev versus kitaev honeycomb cobaltates. *Phys. Rev. B* **107**, 054420, DOI: https://doi.org/10.1103/PhysRevB.107.054420 (2023).

39. Xiang, J. *et al.* Giant magnetocaloric effect in spin supersolid candidate $Na_2BaCo(PO_4)_2$. *Nature* **625**, 270–275, DOI: https://doi.org/10.1038/s41586-023-06885-w (2024).

40. Popescu, T. *et al.* Zeeman split kramers doublets in spin-supersolid candidate $Na_2BaCo(PO_4)_2$. *Phys. Rev. Lett.* **134**, 136703, DOI: DOI:https://doi.org/10.1103/PhysRevLett.134.136703 (2025).

41. Sheng, J. *et al.* Continuum of spin excitations in an ordered magnet. *The Innov.* DOI: https://doi.org/10.1016/j.xinn.2024.100769 (2025).

42. Woodland, L., Okuma, R., Stewart, J. R., Balz, C. & Coldea, R. From continuum excitations to sharp magnons via transverse magnetic field in the spin-$\frac{1}{2}$ ising-like triangular lattice antiferromagnet $na_2BaCo(PO_4)_2$. *Phys. Rev. B* **112**, 104413, DOI: 10.1103/1pvl-kzjm (2025).

43. Zhong, R., Guo, S. & Cava, R. Frustrated magnetism in the layered triangular lattice materials $K_2Co(SeO_3)_2$ and $Rb_2Co(SeO_3)_2$. *Phys. Rev. Mater.* **4**, 084406, DOI: https://doi.org/10.1103/PhysRevMaterials.4.084406 (2020).

44. Noh, J. D. & Kim, D. Phase boundary and universality of the triangular lattice antiferromagnetic Ising model. *Int. J. Mod. Phys. B* **6**, 2913–2924, DOI: https://doi.org/10.1142/S0217979292002309 (1992).

45. Wu, F.-Y. The Potts model. *Rev. Mod. Phys.* **54**, 235, DOI: https://doi.org/10.1103/RevModPhys.54.235 (1982).

46. Metcalf, B. Phase diagram of a nearest neighbor triangular antiferromagnet in an external field. *Phys. Lett. A* **45**, 1–2, DOI: https://doi.org/10.1016/0375-9601(73)90477-5 (1973).

47. Schick, M., Walker, J. & Wortis, M. Antiferromagnetic triangular ising model. *Phys. Lett. A* **58**, 479–480, DOI: https://doi.org/10.1016/0375-9601(76)90491-6 (1976).

48. Sheng, J. *et al.* Two-dimensional quantum universality in the spin-1/2 triangular-lattice quantum antiferromagnet $Na_2BaCo(PO_4)_2$. *Proc. Natl. Acad. Sci.* **119**, e2211193119, DOI: https://doi.org/10.1073/pnas.2211193119 (2022).

49. Gao, Y. *et al.* Spin supersolidity in nearly ideal easy-axis triangular quantum antiferromagnet $Na_2BaCo(PO_4)_2$. *npj Quantum Mater.* **7**, 89, DOI: https://doi.org/10.1038/s41535-022-00500-3 (2022).

50. Miyashita, S. & Kawamura, H. Phase transitions of anisotropic Heisenberg antiferromagnets on the triangular lattice. *J. Phys. Soc. Jpn.* **54**, 3385–3395, DOI: https://doi.org/10.1143/JPSJ.54.3385 (1985).

51. Miyashita, S. Magnetic properties of Ising-like Heisenberg antiferromagnets on the triangular lattice. *J. Phys. Soc. Jpn.* **55**, 3605–3617, DOI: https://doi.org/10.1143/JPSJ.55.3605 (1986).

52. Sheng, Q. & Henley, C. L. Ordering due to disorder in a triangular heisenberg antiferromagnet with exchange anisotropy. *J. Physics: Condens. Matter* **4**, 2937, DOI: https://doi.org/10.1088/0953-8984/4/11/020 (1992).

53. Ulaga, M., Kokalj, J., Wietek, A., Zorko, A. & Prelovšek, P. Finite-temperature properties of the easy-axis heisenberg model on frustrated lattices. *Phys. Rev. B* **109**, 035110, DOI: https://doi.org/10.1103/PhysRevB.109.035110 (2024).

54. Toth, S. & Lake, B. Linear spin wave theory for single-q incommensurate magnetic structures. *J. Physics: Condens. Matter* **27**, 166002, DOI: 10.1088/0953-8984/27/16/166002 (2015).

55. Collins, M. & Petrenko, O. Review/synthèse: triangular antiferromagnets. *Can. journal physics* **75**, 605–655, DOI: https://doi.org/10.1139/p97-007 (1997).

56. Allan, G. & Betts, D. The temperature and frequency dependence of the inelastic neutron scattering from an ising magnet. *Can. J. Phys.* **46**, 799–802, DOI: https://doi.org/10.1139/p68-099 (1968).

57. Muttalib, K. & Barry, J. Inelastic neutron scattering from a geometrically frustrated ising antiferromagnet: Exact solutions. *Phys. Rev. B* **110**, 024414, DOI: https://doi.org/10.1103/PhysRevB.110.024414 (2024).

58. Zhu, M. *et al.* Continuum excitations in a spin supersolid on a triangular lattice. *Phys. Rev. Lett.* **133**, 186704, DOI: https://doi.org/10.1103/PhysRevLett.133.186704 (2024).

59. Goldstone, J., Salam, A. & Weinberg, S. Broken symmetries. *Phys. Rev.* **127**, 965, DOI: https://doi.org/10.1103/PhysRev.127.965 (1962).

60. Weinberg, S. Approximate symmetries and pseudo-goldstone bosons. *Phys. Rev. Lett.* **29**, 1698, DOI: https://doi.org/10.1103/PhysRevLett.29.1698 (1972).

61. Rau, J. G., McClarty, P. A. & Moessner, R. Pseudo-goldstone gaps and order-by-quantum disorder in frustrated magnets. *Phys. Rev. Lett.* **121**, 237201, DOI: https://doi.org/10.1103/PhysRevLett.121.237201 (2018).

62. Gao, Y. *et al.* Double magnon-roton excitations in the triangular-lattice spin supersolid. *Phys. Rev. B* **110**, 214408, DOI: https://doi.org/10.1103/PhysRevB.110.214408 (2024).

63. Jia, H., Ma, B., Wang, Z. & Chen, G. Quantum spin supersolid as a precursory dirac spin liquid in a triangular lattice antiferromagnet. *Phys. Rev. Res.* **6**, 033031, DOI: https://doi.org/10.1103/PhysRevResearch.6.033031 (2024).

64. Zhu, M. *et al.* Wannier states and spin supersolid physics in the triangular antiferromagnet $K_2Co(SeO_3)_2$. *npj Quantum Mater.* **10**, 74, DOI: https://doi.org/10.1038/s41535-025-00791-2 (2025).

65. Xu, Y., Hasik, J., Ponsioen, B. & Nevidomskyy, A. H. Simulating spin dynamics of supersolid states in a quantum ising magnet. *Phys. Rev. B* **111**, L060402, DOI: https://doi.org/10.1103/PhysRevB.111.L060402 (2025).

66. Flores-Calderón, R., Moessner, R. & Pollmann, F. Unconventional spin dynamics and supersolid excitations in the triangular-lattice XXZ model. *arXiv preprint arXiv:2506.15516* (2025).

67. Mauri, A. & Mila, F. Slow convergence of spin-wave expansion and magnon dispersion in the 1/3 plateau of the triangular XXZ antiferromagnet. *Phys. Rev. B* **111**, L180402, DOI: https://doi.org/10.1103/PhysRevB.111.L180402 (2025).

68. Ulaga, M., Kokalj, J., Tohyama, T. & Prelovšek, P. Easy-axis heisenberg model on the triangular lattice: From a supersolid to a gapped solid. *Phys. Rev. B* **111**, 174442, DOI: https://doi.org/10.1103/PhysRevB.111.174442 (2025).

69. Ulaga, M., Kokalj, J., Tohyama, T. & Prelovšek, P. The anisotropic heisenberg model close to the ising limit: triangular lattice vs. effective models. *arXiv preprint arXiv:2510.12667* DOI: https://doi.org/10.48550/arXiv.2510.12667 (2025).

70. Amaral, J. & Amaral, V. On estimating the magnetocaloric effect from magnetization measurements. *J. Magn. Magn. Mater.* **322**, 1552–1557, DOI: https://doi.org/10.1016/j.jmmm.2009.06.013 (2010).

71. Cao, H. *et al.* Demand, a dimensional extreme magnetic neutron diffractometer at the high flux isotope reactor. *Crystals* **9**, 5, DOI: https://doi.org/10.3390/cryst9010005 (2018).

72. Clementi, E. & Roetti, C. Roothaan-hartree-fock atomic wavefunctions: Basis functions and their coefficients for ground and certain excited states of neutral and ionized atoms, $Z \leq 54$. *At. data nuclear data tables* **14**, 177–478, DOI: https://doi.org/10.1016/S0092-640X(74)80016-1 (1974).

73. Tagay, Z., Romero III, R. & Armitage, N. High-precision measurements of terahertz polarization states with a fiber coupled time-domain thz spectrometer. *Opt. Express* **32**, 15946–15954, DOI: https://doi.org/10.1364/OE.516736 (2024).

74. Momma, K. & Izumi, F. Vesta 3 for three-dimensional visualization of crystal, volumetric and morphology data. *J. applied crystallography* **44**, 1272–1276, DOI: https://doi.org/10.1107/S0021889808012016 (2011).

Acknowledgements

We gratefully acknowledge valuable discussions with Gang Chen, Cristian Batista, Yuan Gao, Andreas Läuchli, Wei Li, Changle Liu, Frédéric Mila, Roderich Moessner, Oleg Tchernyshyov, and Shu Zhang. Initial phases of this work were supported as part of the Institute for Quantum Matter, an Energy Frontier Research Center funded by the U.S. Department of Energy, Office of Science, Basic Energy Sciences under Award No. DE-SC0019331. Further neutron scattering work was supported by Department of Energy, Office of Science, Basic Energy Sciences under Award No. DE-SC0024469. C.B. was supported by the Gordon and Betty Moore Foundation EPIQS program under GBMF9456. Y.H. and H.C. were supported by the U.S. Department of Energy, Office of Basic Energy Sciences, Early Career Research Program Award KC0402020. J.Z. acknowledges the support of the NSF CAREER grant DMR-1848349. A portion of this work was performed at the National High Magnetic Field Laboratory, which is supported by the National Science Foundation Cooperative Agreement No. DMR-2128556*, the U.S. Department of Energy, and the State of Florida. This research used resources at the High Flux Isotope Reactor and Spallation Neutron Source, DOE Office of Science User Facilities operated by Oak Ridge National Laboratory. The beam time was allocated to HYSPEC and CNCS on proposal number IPTS-29655. The beam time was allocated to HB-3A on proposal number IPTS-31928.

Author Contributions

T.C., R.Z., and C.B. initiated this work. A.G., X.X., and R.C. prepared the samples. T.C., Y.C., Y.H., H.C., B.L.W., A.A.P., and D.M.P. carried out neutron scattering experiments. A.G., E.C., M.J., and M.L. measured high-field magnetization. L.S., Z.T., and N.P.A. performed THz measurements. T.C., A.G., J.Z., L.C., and C.B. wrote the manuscript with input from all coauthors.

Competing Interests

The authors declare no competing interests.

Figures

Figure 1. Elastic neutron scattering from $K_2Co(SeO_3)_2$ and the inferred magnetic orders. (a-c) Elastic magnetic scattering as a function of momentum, measured at $T = 0.1$ K and shown after subtracting the nuclear background scattering acquired at 12 K. (a) shows scattering at 0 T (top right) and 7 T (bottom left). (b) shows 0 T data, while (c) shows 7 T data with the magnetic field applied along the easy **c**-axis. (d) Calculated and measured l dependence of magnetic neutron scattering for $\mathbf{Q} = (\frac{1}{3}\,\frac{1}{3}\,l)$ and $(\frac{2}{3}\,\frac{2}{3}\,l)$. Solid lines are fits of the "Y" order with $m_\perp/m_z = 0.0(1)$ and $\alpha = 0.049(7)$ (Eq. 5). The dashed line shows the expected intensity from a purely transverse component $m_\perp \neq 0$ ($m_z = 0$ and $\alpha = 0$), calculated using Eq. 5. (e) In-plane correlation length, ξ(in units of the lattice constant a), and squared staggered magnetization (intensity) as functions of temperature. The data were obtained from fits to elastic neutron scattering data acquired on HYSPEC covering an area of the $(hk0)$ plane surrounding $(\frac{1}{3}\,\frac{1}{3}\,l)$ with $|l| < 0.4$. Open and closed cycles indicate data taken with $E_i = 9.0$ and 3.8 meV, respectively with $|\hbar\omega| < 0.5$ meV. Dashed lines are guides to the eye. See SI for details. Error bars in (d, e) indicate the standard deviation. (f-h) Schematic diagrams and temperature regimes of the candidate symmetry-breaking supersolid "Y", $\frac{\mathrm{U}}{2}\,\frac{\mathrm{U}}{2}\mathrm{D}$, and UD0 orders discussed in the text, created by VESTA.[74]

Figure 2. Temperature dependence of magnetization and specific heat capacity, and phase diagram for $K_2Co(SeO_3)_2$**.** (a) Specific heat capacity as a function of temperature, with curves systematically shifted in proportion to the applied field. The zero-field specific heat capacity is reproduced with permission.[43] (b) Magnetization versus temperature for **c**-axis-oriented DC fields up to 30 T. (c) Interpolated color contour plot of differential susceptibility, dM/dT, versus magnetic field and temperature for $\mathbf{H} \parallel \mathbf{c}$ inferred from the data in (b). The labels UUU, UUD, SS, and PM represent the Up-Up-Up (field-polarized), Up-Up-Down, supersolid, and paramagnetic phases, respectively. The inset shows dM/dT as a function of temperature in a 17.5 T field. The data point on the UUD phase boundary at the lowest temperature was determined from a peak in an isothermal measurement of $C_p(H)$. (d) Contour plot of the magnetic entropy change, $\Delta S_m(T,H)$, normalized by the total entropy $R\ln 2$. The map was constructed by first calculating the isothermal change in entropy, $\Delta S_m(T,H)$, from $dM(H)/dT$ using a Maxwell relation.[70] The data were combined with $\Delta S_m(T,H=0)$ inferred from zero field specific heat capacity data to obtain $\Delta S_m(T,H)/R\ln 2$ (see SI).

Figure 3. Magnetic field dependence of magnetization and specific heat capacity, and phase diagram for $K_2Co(SeO_3)_2$**.** (a) Magnetization versus **c**-axis-oriented field at various temperatures down to $T = 0.5$ K. (b) Differential susceptibility dM/dH versus field. (c) Specific heat capacity versus field up to $\mu_0 H = 14$ T at various temperatures. (d) Low-field specific heat capacity as a function of field for temperatures near $T = 4.5$ K. Data are systematically shifted in proportion to temperature to show the onset of a sharp transition. (e) Contour plot of magnetic specific heat capacity C_m versus field and temperature. The field-independent lattice contribution to the specific heat capacity was fitted by the Debye model and subtracted from C_p. The second-order phase transition defined by peak positions in C_p versus temperatures (Fig. 2a) and field (Fig. 3c, d) appears to terminate at (T, $\mu_0 H$) = (4.5 K, 1.1 T). The labels UUD, SS, and PM represent the Up-Up-Down, supersolid, and paramagnetic phases, respectively. Data in the temperature window from 0.3 K to 1.9 K are reproduced with permission.[43]

Figure 4. Magnetic neutron scattering from coherent spin waves in the UUD phase of $K_2Co(SeO_3)_2$. (a) The $(\mathbf{Q}, \omega)$-dependence of the magnetic neutron scattering cross section along high-symmetry directions in a 7 T magnetic field applied along the **c**-axis at $T = 0.1$ K. The path through the Brillouin zone is illustrated in the inset. Data are averaged along the l direction, except for the M_1-L_1 cut along l. The in-plane $\mathbf{Q}$ integration window is ± 0.15 Å^{-1} perpendicular to the trajectory. (b) The neutron scattering cross section for $K_2Co(SeO_3)_2$ in a 7 T field calculated using linear spin-wave theory, as implemented in SpinW.[54] The parameters $J_z = 2.96(2)$ meV and $J_\perp = 0.21(3)$ meV in Eqn. 1 were determined by performing a pixel-to-pixel fit of this model to the measured spectrum in panel (a).

Figure 5. Zero field magnetic excitations in $K_2Co(SeO_3)_2$ probed by magnetic neutron scattering. (a) The $(\mathbf{Q}, \omega)$-dependence of the magnetic neutron scattering cross section along high-symmetry directions in zero field at $T = 0.1$ K acquired with E_i = 9.0 meV neutrons. To obtain the zero-field magnetic scattering, two different backgrounds (BKGs) were subtracted: data from 7 T measurement for $\hbar\omega \leq 2.5$ meV, and a constant value for $\hbar\omega > 2.5$ meV, respectively. The in-plane $\mathbf{Q}$ integration window is ± 0.15 Å^{-1} perpendicular to the trajectory. (b, c) Magnetic neutron scattering as a function of momentum in the $(hk0)$ plane for energy transfers $\hbar\omega = 3$ meV and 6 meV, respectively. A constant background was subtracted from the data. The energy integration window is ± 0.5 meV. (d) The $(\mathbf{Q}, \omega)$-dependence of the magnetic neutron scattering cross section along high-symmetry directions at $T = 0.29$ K obtained with $E_i = 1.0$ meV neutrons. The in-plane $\mathbf{Q}$ integration window is ± 0.05 Å^{-1} perpendicular to the trajectory. (e, f) Low energy magnetic neutron scattering as a function of momentum in the $(hk0)$ plane for six values of $\hbar\omega$. The energy integration window is ± 0.03 meV. All data shown in (a-f) have been integrated along the l direction, which is justified by the quasi-2D character of the magnetic correlations.

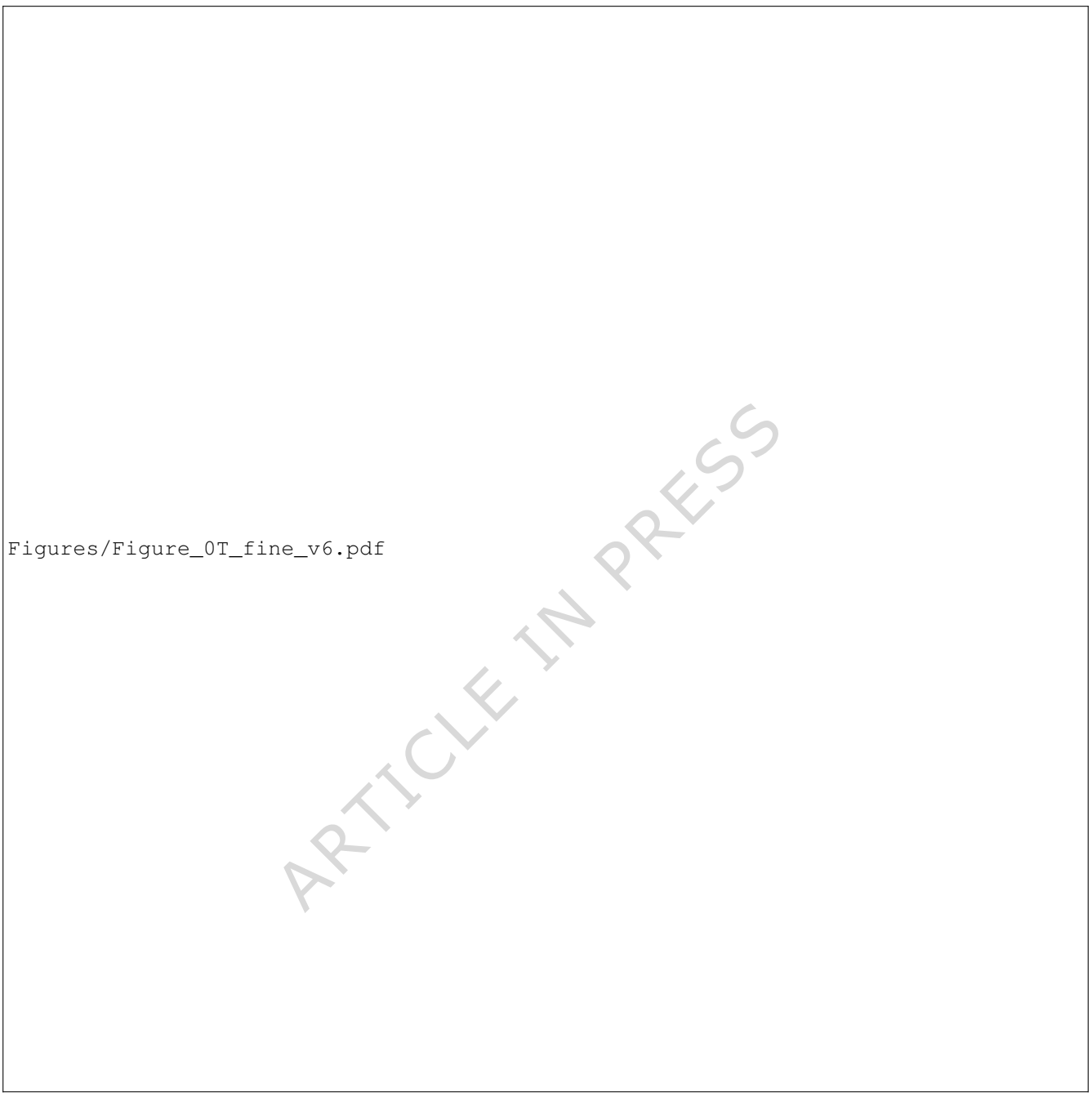

Figure 6. Zero field magnetic excitations around the K point in $K_2Co(SeO_3)_2$**.** (a) The $(\mathbf{Q}, \omega)$-dependence of the magnetic neutron scattering cross section along (hh) at $T = 0.29$ K measured with $E_i = 0.72$ meV. The in-plane $\mathbf{Q}$ integration window is ± 0.05 Å^{-1} perpendicular to the trajectory. Incoherent elastic scattering has been subtracted. (b, c) Linear and logarithmic plots of constant-$\mathbf{Q}$ cut at the K point. The red data points were obtained by averaging the data in (a) over the (hh) range indicated by the white dashed lines. The solid black curves represent the optimal fit including a gapless and a gapped mode based on convoluting Eq. 2 with the experimental energy resolution. The black data points and dashed lines indicate background subtracted incoherent elastic scattering scaled to match the integrated intensity of the magnetic Bragg peak. Therefore, the scattering beyond the dashed lines is predominantly magnetic. The inset of (c) shows χ^2, quantifying the fit quality, as a function of Γ_{QE} and $\Gamma_{QE} \cdot \chi_0$, which is a measure of the integrated intensity of the quasi-elastic component. The red dot indicates the minimal value for χ^2. All data shown have been integrated along the l direction. The labels E, QE, and DHO represent the elastic, quasi-elastic, and damped harmonic oscillator contributions, respectively. Error bars indicate the standard deviation.

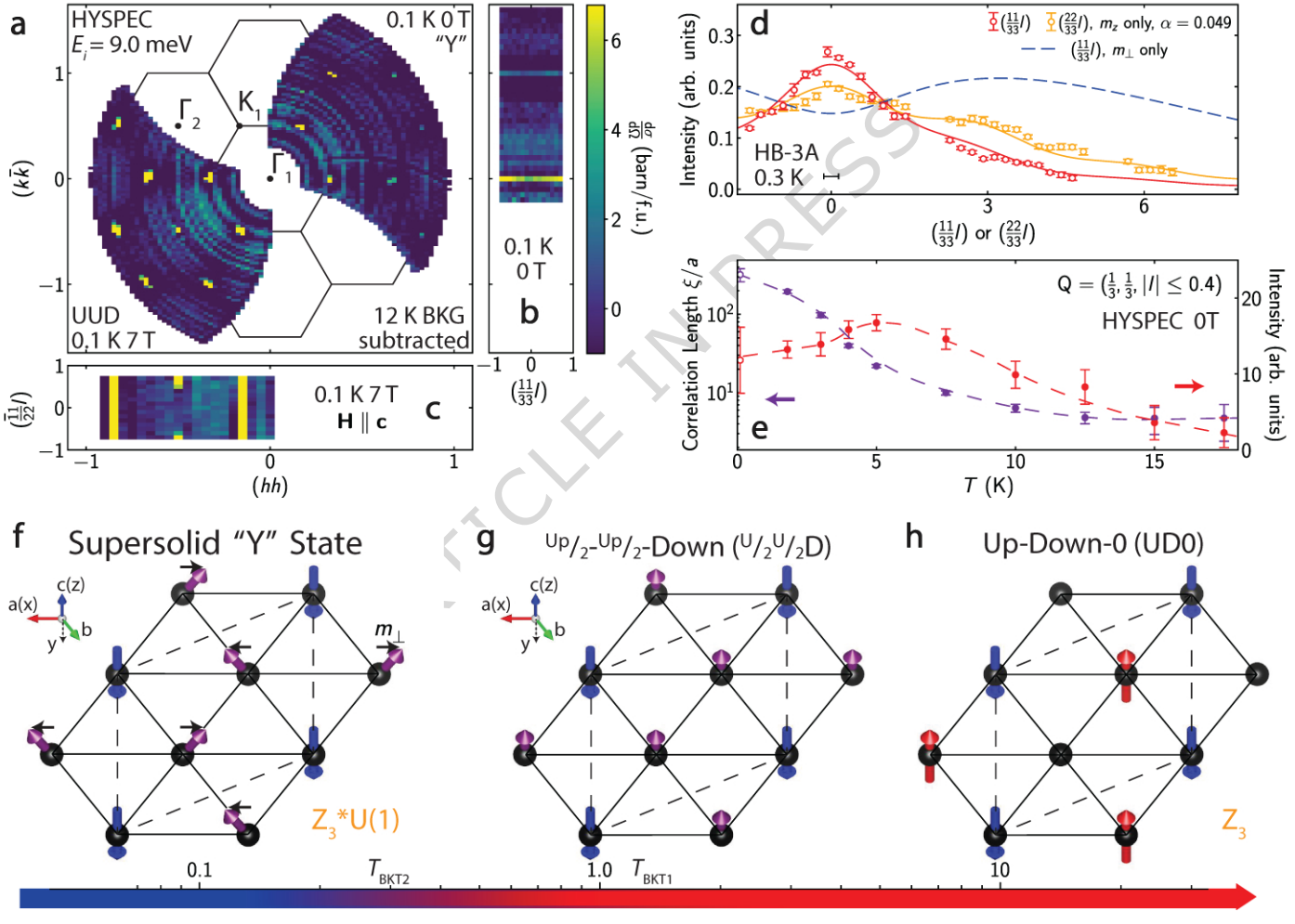
a
HYSPEC
E_i = 9.0 meV
0.1 K 0 T
"Y"
Γ_2
K_1
Γ_1
UUD
0,1 K 7 T
12 K BKG
subtracted
$(k\bar{k})$
0.1 K
0 T
b
$\frac{d\sigma}{d\Omega}$ (barn/f.u.)
0.1 K 7 T
H ∥ c
c
$(\frac{11}{22}l)$
(hh)
$(\frac{11}{33}l)$
d
$(\frac{11}{33}l)$
$(\frac{22}{33}l)$, m_z only, $\alpha = 0.049$
$(\frac{11}{33}l)$, $m_\perp$ only
HB-3A
0.3 K
Intensity (arb. units)
$(\frac{11}{33}l)$ or $(\frac{22}{33}l)$
e
Correlation Length ξ/a
Q = $(\frac{1}{3}, \frac{1}{3}, |l| \leq 0.4)$
HYSPEC 0T
Intensity (arb. units)
T (K)
f
Supersolid "Y" State
c(z)
a(x)
b
y
$m_\perp$
Z_3*U(1)
0.1
T_{BKT2}
g
$^{Up}/_2$-$^{Up}/_2$-Down ($^U/_2{}^U/_2$D)
1.0
T_{BKT1}
h
Up-Down-0 (UD0)
Z_3
10

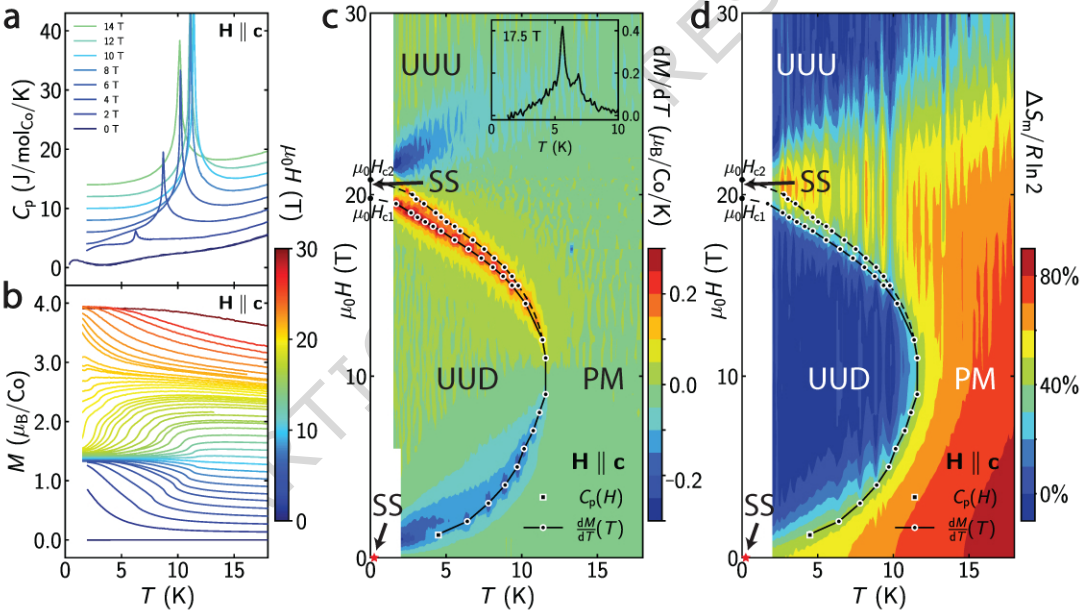
a
b
c
d
14 T
12 T
10 T
8 T
6 T
4 T
2 T
0 T
H ∥ c
C_p (J/mol$_{Co}$/K)
M (μ_B/Co)
T (K)
$\mu_0 H$ (T)
UUU
UUD
PM
SS
$\mu_0 H_{c2}$
$\mu_0 H_{c1}$
17.5 T
$C_p(H)$
$\frac{dM}{dT}(T)$
dM/dT (μ_B/Co/K)
$\Delta S_m/R \ln 2$
80%
40%
0%

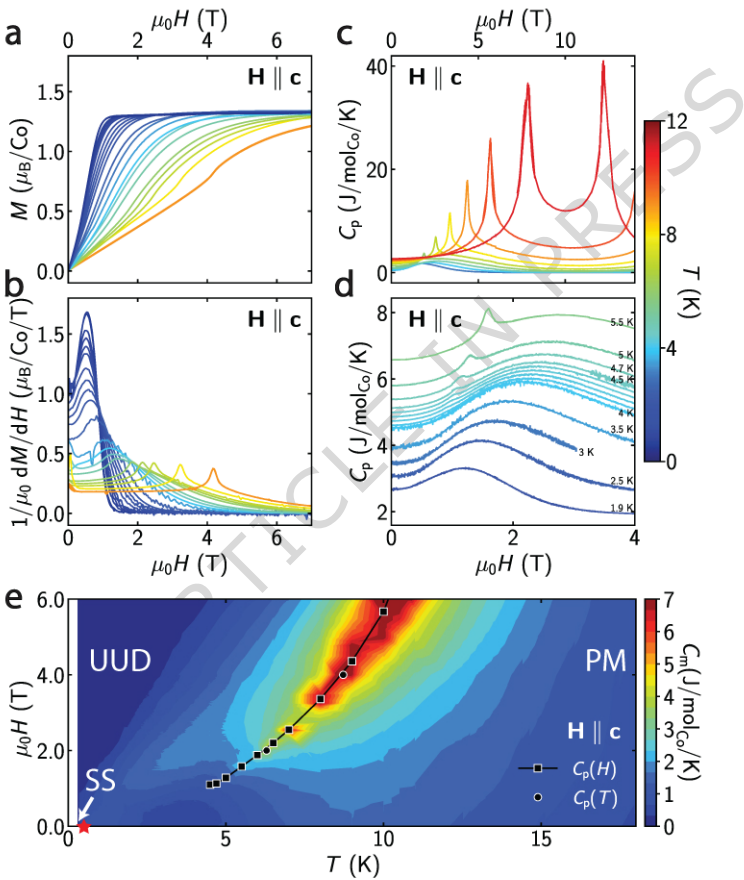

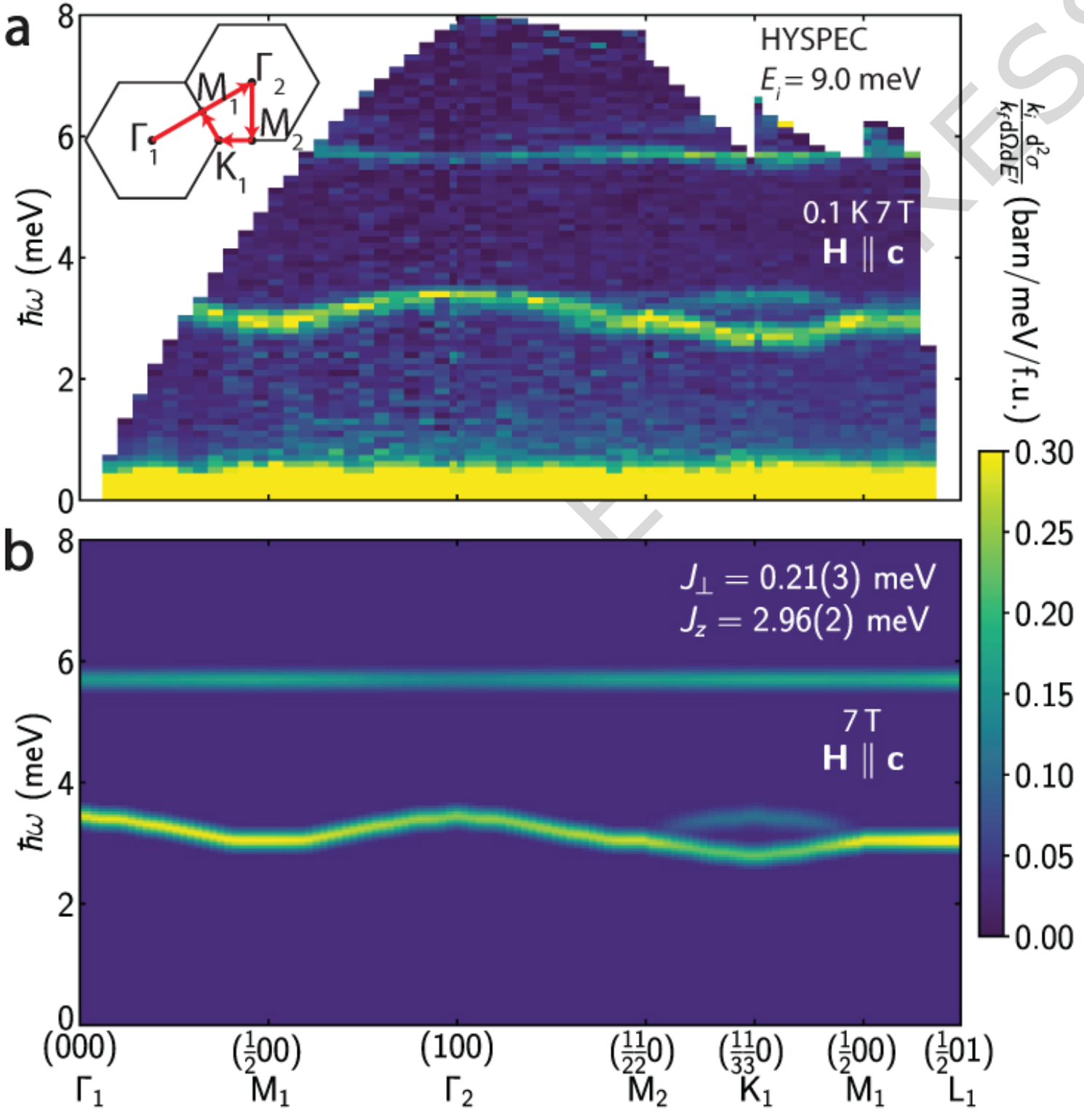

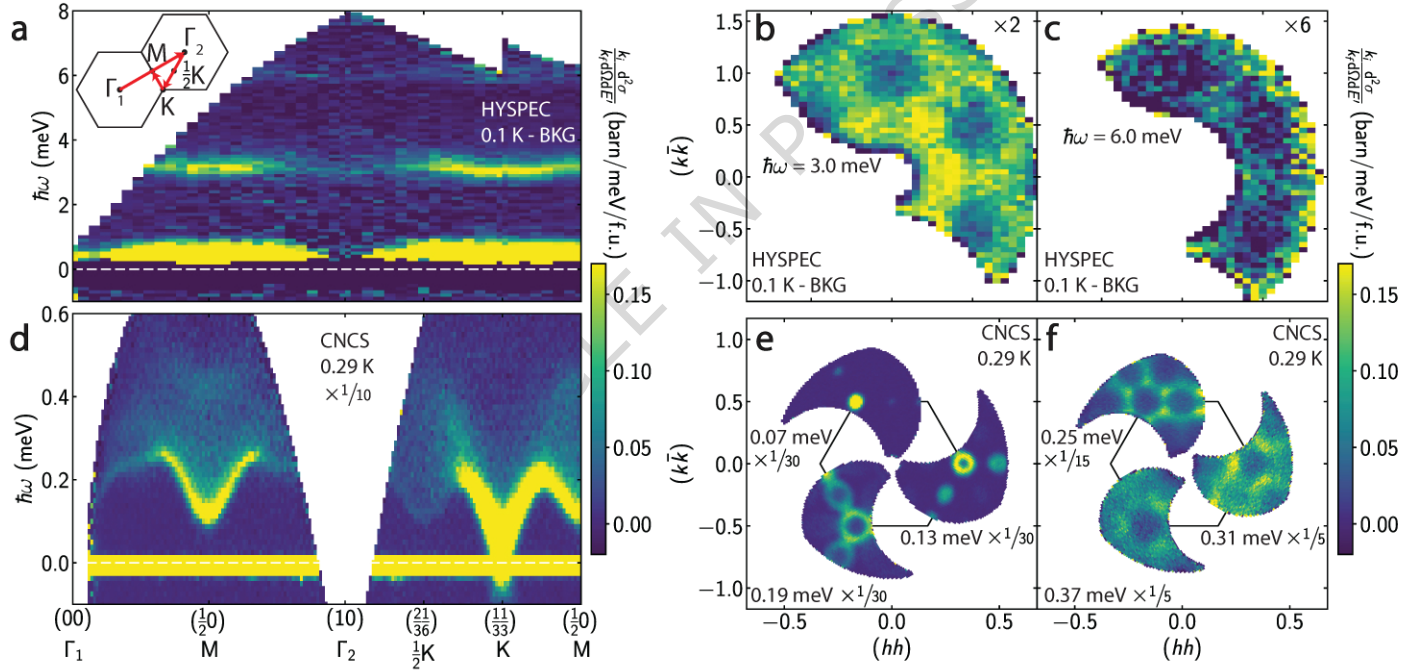
a
b
c
d
e
f
HYSPEC
0.1 K - BKG
CNCS
0.29 K
×1/10
×2
×6
ħω = 3.0 meV
ħω = 6.0 meV
0.07 meV
×1/30
0.13 meV ×1/30
0.19 meV ×1/30
0.25 meV
×1/15
0.31 meV ×1/5
0.37 meV ×1/5
ħω (meV)
(kk̄)
(hh)
Γ1
M
Γ2
½K
K
(00)
(10)
(21/36)
(11/33)
(½0)
$\frac{k_i}{k_f}\frac{d^2\sigma}{d\Omega dE'}$ (barn/meV/f.u.)